PCCP

ROYAL SOCIETY OF CHEMISTRY

PAPER

View Article Online
View Journal | View Issue

Cite this: *Phys. Chem. Chem. Phys.*, 2025, **27**, 17922

Observation of double-ring tubular $B_{20}(CO)_n^+$ (n = 1–8): emergence of 2D-to-3D transition in boron carbonyl complexes

Hong Niu, Qiang Chen,* Rui-Nan Yuan, Qin-Wei Zhang and Si-Dian Li*

Received 15th May 2025,
Accepted 24th July 2025

DOI: 10.1039/d5cp01827g

rsc.li/pccp

The consecutive discoveries of double-ring (DR) tubular D_{10d} B_{20} and D_{2d} B_{20}^+ as embryos of single-walled boron nanotubes have attracted considerable attention in the past two decades. Joint chemisorption experiments and first-principles theory investigations performed herein indicate that, as the only isomer of the monocation observed in gas-phase experiments, DR tubular D_{2d} B_{20}^+ can react with CO successively under ambient conditions to form a series of DR tubular boron carbonyl monocations $B_{20}(CO)_n^+$ up to n = 8, presenting the largest boron carbonyl complexes observed to date, which mark the 2D-to-3D transition in boron carbonyl complexes. DR tubular D_{2d} B_{20}^+ with twenty peripheral boron atoms is found to be about ten times more reactive to chemisorb the first CO than the experimentally known quasi-planar C_{2v} B_{13}^+ (B_3@B_{10}^+) with typical π-aromaticity analogous to benzene's but about ten times less reactive than both quasi-planar C_s B_{11}^+ (B_2@B_9^+) and C_{2v} B_{15}^+ (B_4@B_{11}^+) with σ and π conflicting aromaticity. Extensive theoretical calculations and analyses unveil the chemisorption pathways, potential energy profiles, and chemical bonding patterns of DR tubular $B_{20}(CO)_n^+$ and its neutral counterpart $B_{20}(CO)_n$, both of which appear to be tubularly aromatic in nature.

Introduction

Carbon monoxide (CO) is one of the most important ligands in chemistry due to its unique capacity to form σ-donation and π-back-donation coordination interactions in metal carbonyl complexes.[1–3] In typical transition-metal (TM) carbonyl complexes, the :C≡O ligand donates its σ-HOMO lone-pair on carbon to the partially occupied (n − 1)d orbitals of the TM center while concurrently accepting back donation from the (n − 1)d orbitals of the TM center in its two degenerate π*-LUMO antibonding orbitals. σ + π dual coordination interactions dominate the electronic structures and reactivities of TM carbonyl complexes. Main group metal carbonyl complexes have also been discovered in the past decade, including the cubic alkaline-earth metal carbonyl complexes $M(CO)_8$ (M = Ca, Sr, and Ba) and $Be(CO)_n$ (n = 1–4), in which the alkaline-earth metals serve as "honorable transition metals" exhibiting transition-metal-like behaviors.[4,5]

As a prototypical electron-deficient element in the periodic table, boron (He[$2s^2 2p^1$]) can also form various types of carbonyl complexes. The closed-shell carbonyl borane H_3BCO and its derivatives are experimentally known as stable boron carbonyl complexes.[6] In recent years, various small boron carbonyl clusters, including linear BCO,[7] OCBBCO,[8] and BBCO,[9] V-shaped $B(CO)_2$,[10] rhombic $B_4(CO)_2$,[11] and planar (2D) $B(CO)_3^+$, $B(CO)_4^+$, $B_2(CO)_4^+$, and $B_3(CO)_n^+$ (n = 3–6), have been observed in experiments using infrared photodissociation (IRPD) spectroscopy.[12–15] Neutral rhombic $B_4(CO)_3$ was also observed in the gas phase.[16] In these boron carbonyl complexes, CO ligands serve as donors to coordinate B_n centres as acceptors *via* effective σ-donations. Based on joint gas-phase mass spectroscopy, collision-induced dissociation (CID), and first-principles theory investigations, our group observed in 2024 the first quasi-planar boron carbonyl aromatics (BCAs) $B_{13}(CO)_n^+$ (n = 1–7), analogous to benzene C_6H_6 under ambient conditions.[17] CID experiments confirmed that CO ligands are molecularly coordinated to the aromatic B_{13}^+ core in these BCAs without being activated or disassociated. Similarly, in 2025, quasi-planar $B_{11}(CO)_n^+$ (n = 1–6) and $B_{15}(CO)_n^+$ (n = 1–5) with π and σ conflicting aromaticity were observed in the gas phase, presenting the largest boron carbonyl complexes observed to date.[18] Neutral double-ring tubular $B_{20}(CO)_n$ (n = 1–8) complexes based on the framework of aromatic DR tubular B_{20} have also been predicted in theory recently.[19] However, to the best of our knowledge, there have been no three-dimensional (3D) boron carbonyl complexes observed to date in experiments, leaving an important question to be addressed in this area.

Based on the fact that neutral B_{20} has a perfect double-ring (DR) tubular D_{10d} structure as its well-defined global minimum

Institute of Molecular Science, Shanxi University, Taiyuan 030006, P. R. China. E-mail: chenqiang@sxu.edu.cn, lisidian@sxu.edu.cn

(GM),[20–22] B_{20}^+ monocation possesses a slightly distorted DR tubular D_{2d} configuration as its deep-lying GM, which was the only stable isomer of the system observed in ion-mobility experiments.[23] While both of them can be considered as the embryos of single-walled boron nanotubes, we report herein the observation of a series of DR tubular boron carbonyl monocations $B_{20}(CO)_n^+$ (n = 1–8) in gas phase under ambient conditions, as revealed by detailed chemisorption experiments and extensive first-principles theory calculations, presenting the largest boron carbonyl complexes observed to date, which mark the 2D-to-3D structural transition in boron carbonyl complexes. DR tubular D_{2d} B_{20}^+ with twenty periphery boron atoms was found to be much more reactive to chemisorb the first CO than the previously reported planar π-aromatic C_{2v} B_{13}^+, but much less reactive than both 2D C_s B_{11}^+ ($B_2@B_9^+$) and C_{2v} B_{15}^+ ($B_4@B_{11}^+$) with σ and π conflicting aromaticity. Detailed theoretical calculations and analyses reveal the chemisorption mechanisms and bonding patterns of the experimentally observed DR tubular $B_{20}(CO)_n^+$ monocations and their neutral DR tubular counterparts $B_{20}(CO)_n$ (n = 1–8), with both appearing to be aromatic in nature.

Methods

Experimental methods

A homemade reflection time-of-flight mass spectrometer (TOF-MS)[17,18,24,25] equipped with a laser ablation cluster source, a quadrupole mass filter (QMF),[26] and a linear ion trap (LIT)[27] reactor was employed in this work. Bare boron cluster monocations (B_n^+) were generated by laser ablation of a rotating and translating ^{11}B target (99% enriched) under a 6 atm He carrier gas. A 532 nm pulsed laser (Nd^{3+}:YAG second harmonic) with an energy of 3–5 mJ per pulse and a repetition rate of 10 Hz was used to ablate the boron target.

B_{20}^+ monocations were mass-selected by the QMF and entered into the LIT, where they were confined and thermalized by collisions with a pulse of He gas and then interacted with a pulse of CO reactant gas. The cluster ions ejected from the LIT reactor were detected using TOF-MS. The pseudo-first-order rate constants (k_1) of the reaction between B_{20}^+ and CO were determined using the following equation,

$$\ln\frac{I_R}{I_T} = -k_1\frac{P_{effective}}{k_B T}t_R \quad (1)$$

in which I_R is the signal intensity of the reactant cluster ions after the reaction, I_T is the total ion intensity including contributions from the products, $P_{effective}$ is the effective pressure of the reactant gas in the ion trap reactor, k_B is the Boltzmann constant, T is the temperature ($\sim$300 K), and t_R is the reaction time. More details about the method to derive k_1 can be found in ref. 28.

Theoretical methods

Extensive density functional theory (DFT) calculations at the PBE0/6-311+G(d) level[29,30] were performed using the Gaussian 16 program.[31] Previous CID experiments on BCAs $B_{13}(CO)_n^+$ indicate that CO ligands in boron carbonyl complexes are coordinated molecularly to the peripheral atoms of the B_m^+ cores, without being activated or dissociated.[17] Using CO as molecular ligands to coordinate the experimentally observed DR tubular D_{2d} B_{20}^+ core, which is the only stable isomer of the monocation existing in the gas phase,[23] the structures of the $B_{20}(CO)_n^+$ (n = 1–8) boron carbonyl complexes, intermediates (IMs), and transition states (TSs) were extensively manually constructed and fully optimized in this work. The hybrid PBE0 functional, which has proven to be reliable for boron cluster calculations,[17,18,32–34] was employed in this work. Vibrational frequency analyses confirmed that all IMs and TSs were true minima and transition states of the systems, respectively. Intrinsic reaction coordinate (IRC) calculations[35,36] were further conducted to verify that each TS with one imaginary vibrational frequency (as indicated in Fig. S10–S21) connects two appropriate IMs. Based on the fact that DR tubular D_{2d} B_{20}^+ is the only isomer of the monocation observed in ion-mobility experiments[23] and CO ligands are molecularly coordinated to the $B_m^{+/0}$ cores in CID measurements,[17] the optimized structures obtained herein by extensive manual structural constructions based on D_{2d} B_{20}^+ are believed to be reliable, though no global structural optimization and direct IRPD spectroscopic comparison were performed at the current stage. PBE0-D3/6-311+G(d) structural optimizations with dispersion correction (Becke–Johnson damping D3 correction)[37] included were also performed to compare with the results obtained using PBE0/6-311+G(d). More accurate single-point DLPNO-CCSD(T)[38] calculations were performed on the most favorable chemisorption pathways of the experimentally observed $B_{20}(CO)_n^+$ (n = 1–8) monocations using the ORCA program.[39] Adaptive natural density partitioning (AdNDP 2.0) bonding analyses[40,41] were performed on the concerned species. Iso-chemical shielding surfaces (ICSSs) were computed using the Multiwfn 3.8 program[42] and visualized using the VMD 1.9.3 software.[43] Detailed anisotropies of the current-induced density (ACID) analyses were realized using the ACID 2.0 code[44] to further check the tubular aromaticity of the systems, with the ring current maps finally generated using POV-Ray 3.7 render.[45] In addition, energy decomposition analyses with natural orbitals for chemical valence (EDA-NOCV)[46–48] were performed using the ADF(2023) program package[49] at the PBE0/TZ2P level combined with the zeroth-order regular approximation (ZORA)[50] to elucidate the coordination bonding characteristics of $B_{20}(CO)_n^{+/0}$.

Results and discussion

Cluster reactivity measurements

The TOF mass spectra of the reactions of B_{20}^+ with CO in Fig. 1A indicate that B_{20}^+ can consecutively chemisorb up to eight CO ligands under ambient conditions to form the $B_{20}(CO)_n^+$ (n = 1–8) complex series, presenting the highest coordination number of n = 8 in boron carbonyl complexes observed to date. Upon reacting B_{20}^+ with 356 mPa CO for 2 ms, distinct signals of $B_{20}CO^+$ and $B_{20}(CO)_2^+$ corresponding to the first and second CO

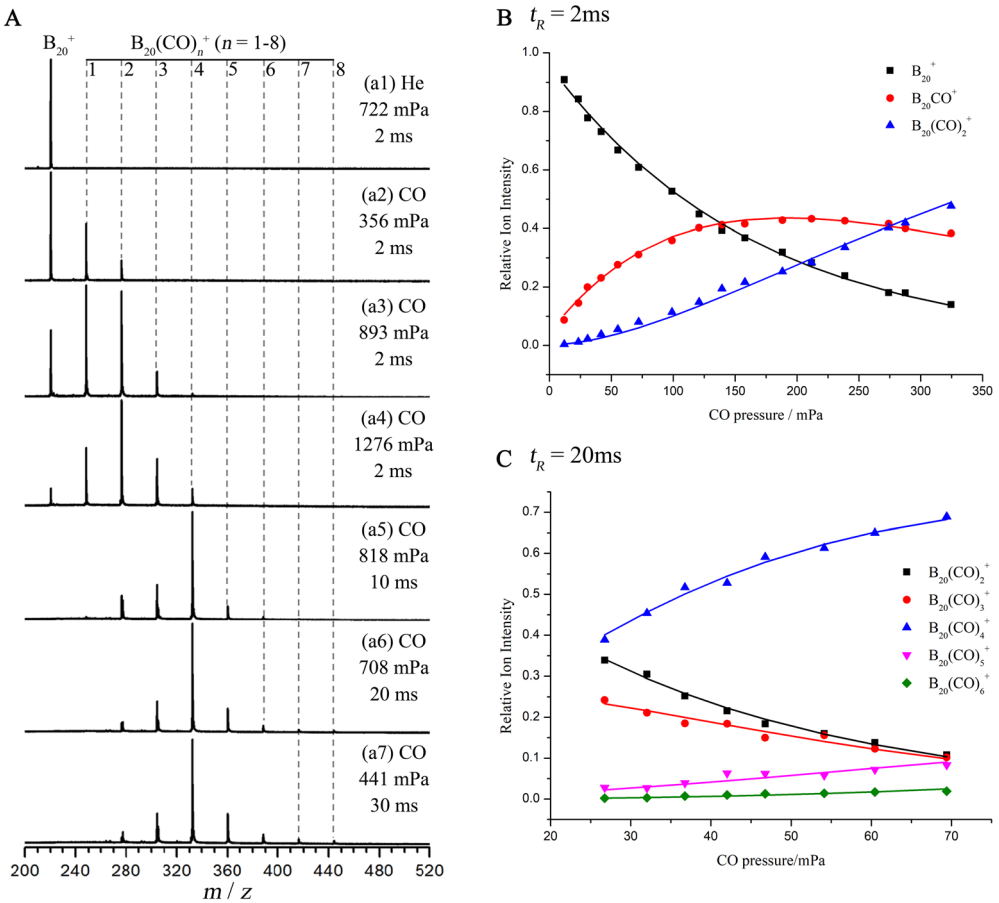

Fig. 1 (A) Measured TOF mass spectra for the reactions of mass-selected B_{20}^+ with nCO (n = 1–8) and variations in the measured relative signal intensities of the reactant and product ions with respect to CO gas pressures in the reactions of (B) $B_{20}^+ + n\text{CO} \rightarrow B_{20}(\text{CO})_n^+$ (n = 1–2) and (C) $B_{20}(\text{CO})_2^+ + (n-2)\text{CO} \rightarrow B_{20}(\text{CO})_n^+$ (n = 3–6), with the solid lines fitted to experimental data points with the approximation of pseudo-first-order reaction mechanisms.

adsorptions were clearly observed, respectively (Fig. 1(a2)). When the CO pressure was increased to 893 mPa (Fig. 1(a3)), the product $B_{20}(\text{CO})_3^+$ emerged. Increasing the CO pressure to 1276 mPa (Fig. 1(a4)), the signal intensities of both B_{20}^+ and $B_{20}\text{CO}^+$ were significantly reduced, with a weak signal appearing at $B_{20}(\text{CO})_4^+$. To further investigate the chemisorption capacity of B_{20}^+ toward CO, the reaction time was extended to 10 ms (Fig. 1(a5)). Under these conditions, the reactant signal of B_{20}^+ and product signal of $B_{20}\text{CO}^+$ disappeared completely, the $B_{20}(\text{CO})_2^+$ signal was obviously weakened, while the relative intensity of $B_{20}(\text{CO})_4^+$ increased effectively and new product signals of both $B_{20}(\text{CO})_5^+$ and $B_{20}(\text{CO})_6^+$ started to emerge. These results indicate that no inert isomers of B_{20}^+ exist in our experiments. Further prolonging the reaction time to 20 ms (Fig. 1(a6)) and 30 ms (Fig. 1(a7)) led to a notable enhancement of the $B_{20}(\text{CO})_6^+$ signal and the ultimate emergence of both $B_{20}(\text{CO})_7^+$ and $B_{20}(\text{CO})_8^+$. No signal beyond, corresponding to the ninth CO adsorption product ($B_{20}(\text{CO})_9^+$), was detected in our experiments (Fig. 1(a7)). The experimental results observed above show that B_{20}^+ can successively chemisorb up to eight CO molecules in the following chemisorption reaction:

$$B_{20}^+ + n\text{CO} \rightarrow B_{20}(\text{CO})_n^+ \quad (n = 1\text{–}8) \qquad (2)$$

Based on detailed chemisorption measurements and the least-squares fitting procedure of eqn (1), the pseudo-first-order rate constants (k_1) for the reactions of $B_{20}^+ + n\text{CO} \rightarrow B_{20}(\text{CO})_n^+$ (n = 1–2) were estimated to be $k_1 = (2.65 \pm 0.53) \times 10^{-11}$ [ϕ = (1.91 ± 0.38)%] and $(1.84 \pm 0.37) \times 10^{-11}$ [ϕ = (1.33 ± 0.27)%] cm^3 molecule^{-1} s^{-1} for n = 1 and 2, respectively (Fig. 1B). For consecutive chemisorptions of $B_{20}(\text{CO})_2^+$ with more CO molecules to form $B_{20}(\text{CO})_n^+$ (n = 3–6), the k_1 values were estimated to be $k_1 = (5.76 \pm 1.15) \times 10^{-11}$, $(1.10 \pm 0.22) \times 10^{-11}$, $(7.64 \pm 1.53) \times 10^{-13}$, and $(1.95 \pm 0.39) \times 10^{-12}$ cm^3 molecule^{-1} s^{-1} for n = 3, 4, 5, and 6, with the corresponding reaction efficiencies of ϕ = (4.15 ± 0.83)%, (0.79 ± 0.16)%, (0.06 ± 0.01)%, and (0.14 ± 0.03)%, respectively (Fig. 1C). It is noticed that $B_{20}(\text{CO})_4^+$ possesses the highest mass intensity in Fig. 1(a4)–(a7) in the $B_{20}(\text{CO})_n^+$ (n = 2–8) series and exhibits the most abundant accumulative intensity in Fig. 1C in the $B_{20}(\text{CO})_n^+$ (n = 2–6) series. These kinetic results suggest that $B_{20}(\text{CO})_4^+$ possesses a unique structure, which is chemically more stable than its neighbours and relatively less reactive to chemisorb more CO molecules. Previous ion mobility measurements[23] indicate DR tubular D_{2d} B_{20}^+ is the well-defined GM of the monocation and the only stable isomer observed in the gas phase. The k_1 value estimated here shows that the DR tubular D_{2d} B_{20}^+ is about ten

times more reactive to chemisorb the first CO than the typical planar π-aromatic C_{2v} B_{13}^+ analogous to benzene,[17] but about ten times less reactive than both quasi-planar C_s B_{11}^+ and C_{2v} B_{15}^+ with σ and π conflicting aromaticity,[18] suggesting that relative reactivities of the concerned B_n^+ towards the first CO are closely related to the geometries and aromaticities of the systems.

Chemisorption pathway analyses

The optimized lowest-lying isomers and corresponding most favourable chemisorption pathways of $B_{20}(CO)_n^+$ (n = 1–8) monocations and $B_{20}(CO)_n$ (n = 1–8) neutrals are depicted in Fig. 2A and C, respectively. Alternative low-lying isomers and minor chemisorption pathways starting from local minima, which are slightly less stable than the corresponding lowest-lying isomers on the most favourable chemisorption pathways, are collectively shown in Fig. S1–S6 and Fig. S8–S21, respectively. The CO molecular ligands appear to prefer to be chemisorbed along both the top and bottom B_{10} rings of DR tubular $B_{20}^{+/0}$ at two opposite sides. As shown in Fig. 2A, the first CO is coordinated to the top B_{10} ring of DR tubular B_{20}^+ without an energy barrier, forming the most stable adduct C_s $B_{20}(CO)^+$ (**1A**) with a chemisorption energy of 1.08 eV. Therefore, the observed $B_{20}(CO)^+$ mass signal should correspond to C_s $B_{20}(CO)^+$ (**1A**), which represents the most favourable configuration in both thermodynamics and dynamics. Similarly, the experimentally

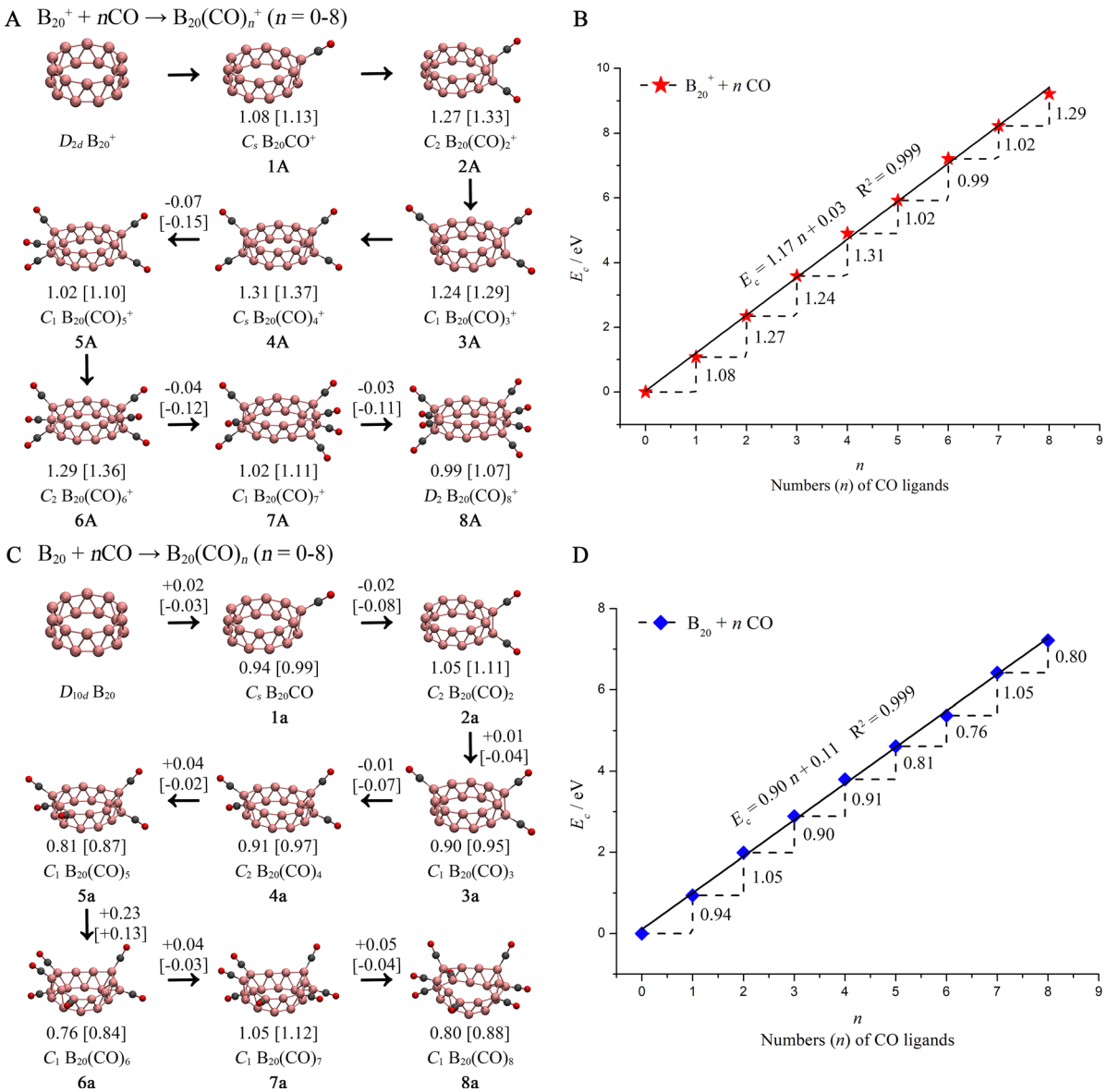

Fig. 2 Optimized structures and chemisorption pathways of (A) $B_{20}(CO)_n^+$ monocations (n = 1–8) and (C) $B_{20}(CO)_n$ neutrals (n = 1–8), with their chemisorption energies and corresponding energy barriers indicated in eV at the PBE0/6-311+G(d) and PBE0-D3/6-311+G(d) (in square brackets) levels, respectively. Variations in the calculated chemisorption energies (E_c) with the numbers (n) of CO ligands in the concerned complexes with respect to (B) $B_{20}^+ + nCO \rightarrow B_{20}(CO)_n^+$ and (D) $B_{20} + nCO \rightarrow B_{20}(CO)_n$ (n = 1–8) at PBE0/6-311+G(d).

observed $B_{20}(CO)_2^+$, $B_{20}(CO)_3^+$, and $B_{20}(CO)_4^+$ can be assigned to C_2 **2A**, C_1 **3A**, and C_s **4A** (Fig. S8), which possess the most favourable chemisorption energies, respectively, *via* barrierless chemisorption processes. We notice that the experimentally observed C_s $B_{20}(CO)_4^+$ (**4A**) can also be formed from the third lowest-lying isomer C_1 $B_{20}(CO)_3^+$ (**3C**) in a barrierless minor chemisorption process (Fig. S9). Notably, with the largest chemisorption energy of 1.31 eV (Fig. 2A) and lowest reaction rate of $k_1 = 7.64 \times 10^{-13}$ cm^3 molecule^{-1} s^{-1}, the observed C_s $B_{20}(CO)_4^+$ (**4A**) with four CO ligands symmetrically distributed at two opposite sites exhibits the highest mass intensity in the $B_{20}(CO)_n^+$ (n = 1–8) series (Fig. 1(a4)–(a7)). The formation of $B_{20}(CO)_5^+$ (**5A**) proceeds through the transition state TS1, which lies 0.07 eV lower than the entrance channel (Fig. 3A and Fig. S10). Further analysis reveals that the adsorption of the sixth CO molecule to form the most stable adduct C_2 $B_{20}(CO)_6^+$ (**6A**) from C_1 $B_{20}(CO)_5^+$ (**5A**) is also a barrierless process (Fig. 2A and Fig. S8). The subsequent chemisorption pathways C_2 $B_{20}(CO)_6$ (**6A**) + CO → C_1 $B_{20}(CO)_7^+$ (**7A**) and C_1 $B_{20}(CO)_7^+$ (**7A**) + CO → D_2 $B_{20}(CO)_8^+$ (**8A**) involve the transition states TS2 and TS3, which lie 0.04 eV and 0.03 eV lower than the entrance channels (Fig. 2A and Fig. S11, S12), respectively, indicating that these processes are also barrierless, with the axially chiral D_2 $B_{20}(CO)_8^+$ (**8A**) possessing the highest symmetry in the series with a symmetrical CO ligand distribution. However, as shown in Fig. S13, further calculations indicate that the chemisorption process of D_2 $B_{20}(CO)_8^+$ (**8A**) + CO → C_1 $B_{20}(CO)_9^+$ (**9A**) possesses a positive energy barrier of +0.15 eV, indicating that the formation of $B_{20}(CO)_9^+$ is kinetically unfavourable under ambient conditions, consistent with the observation that no mass signal of $B_{20}(CO)_9^+$ was detected in experiments (Fig. 1(a7)). As the most favourable chemisorption pathway, the D_{2d} B_{20}^+ → C_s **1A** → C_2 **2A** → C_1 **3A** → C_s **4A** → C_1 **5A** → C_2 **6A** → C_1 **7A** → D_2 **8A** process in Fig. 2A possesses an overall exothermicity of 9.22 eV, enabling the consecutive chemisorptions of eight CO ligands in the $B_{20}(CO)_n^+$ series (n = 1–8). As indicated in Fig. S7, the PBE0 and PBE0-D3 relative energies and energy barriers on the most favourable chemisorption pathway of the experimentally observed $B_{20}(CO)_n^+$ monocations (n = 0–8) are well supported by single-point DLPNO-CCSD(T) calculations, the most accurate calculations performed in this work. Inspiringly, as clearly indicated in Fig. 2(B), the chemisorption energies (E_c) with respect to B_{20}^+ + nCO → $B_{20}(CO)_n^+$ exhibit an almost perfect linear relationship of $E_c = 1.17n + 0.03$ with the number (n) of CO ligands involved in the complexes, with the average chemisorption energy of E_c = 1.17 eV per CO, indicating that DR tubular B_{20}^+ monocation consecutively chemisorbs the eight CO molecular ligands almost independently.

Further PBE0 calculations indicate that, starting from neutral DR tubular D_{10d} B_{20}, which possesses twenty equivalent peripheral boron atoms, the neutral C_s $B_{20}(CO)$ (**1a**) can be formed by overcoming a marginal energy barrier of +0.02 eV, while C_2 $B_{20}(CO)_2$ (**2a**) and C_1 $B_{20}(CO)_4$ (**4a**) can be spontaneously generated *via* barrierless processes (Fig. 2C and Fig. S14, S15, S17). The sequential $B_{20}(CO)_n$ can be achieved by overcoming the small energy barriers of +0.01, +0.04, +0.23, +0.04, and +0.05 eV for n = 3, 5, 6, 7, and 8, respectively (Fig. 2C and Fig. S16, S18–S21), with an overall exothermicity of 7.22 eV. The carbonylation of the typical aromatic neutral DR tubular D_{10d} B_{20} turns out to be both thermodynamically and dynamically less favourable than that of the more electron-deficient DR tubular monocation D_{2d} B_{20}^+. Interestingly, as shown in Fig. 2(D), the chemisorption energies with respect to B_{20} + nCO → $B_{20}(CO)_n$ also exhibit an almost perfect linear relationship $E_c = 0.90n + 0.11$ with the number of CO ligands involved in the systems, with an obviously lower average chemisorption energy of E_c = 0.90 eV per CO. Interestingly, as indicated in Fig. 2, with D3 dispersion corrections included, the PBE0-D3 approach produces similar optimized structures and relative energies with PBE0 for both the $B_{20}(CO)_n^+$ and $B_{20}(CO)_n$ (n = 1–8) series, with PBE0-D3 generating small negative energy barriers for all the concerned chemisorption processes, except $B_{20}(CO)_5$ (**5a**) + CO → $B_{20}(CO)_6$ (**6a**), which has a small positive energy barrier of +0.13 eV.

Bonding pattern and aromaticity analyses

To better understand the high stability of the $B_{20}(CO)_n^{+/0}$ (n = 0–8) series, detailed AdNDP bonding pattern analyses were performed, as shown in Fig. 3 and Fig. S22–S29. Fig. 3 clearly indicates that the perfect DR tubular neutral D_{10d} B_{20} and experimentally observed DR tubular D_{2d} B_{20}^+ possess very similar bonding patterns, which can be categorized into three subgroups. For simplicity, we first discuss the closed-shell neutral D_{10d} B_{20} in Fig. 3A. The first subgroup in B_{20} contains 20 2c-2e localized B–B σ-bonds on the two B_{10} rings with the occupation numbers (ON) of ON = 1.79 |e|. These bonds can also be analysed as 20 3c-2e σ-bonds with slightly higher ON values (1.97 |e|), which are responsible for connecting the two adjacent B_{10} rings, similar to the situation reported in DR tubular $Co@B_{16}^-$.[51] The second group consists of 5 20c-2e σ + σ bonds with ON = 2.00 |e|, which represent in-phase orbital overlaps between the two adjacent B_{10} rings. These completely delocalized σ-bonds match the $4n + 2$ Hückel rule (n = 2) and render σ-aromaticity to DR tubular D_{10d} B_{20}. The third group possesses 5 completely delocalized 20c-2e π + π bonds formed positively between the two B_{10} rings with ON = 2.00 |e|, which match the $4n + 2$ Hückel rule (n = 2) and make the system π-aromatic in nature. As clearly shown in Fig. 3B, the slightly distorted open-shell D_{2d} B_{20}^+ possesses a bonding pattern very similar to that of neutral D_{10d} B_{20}, with the only difference occurring at the last delocalized 20c-2e π + π bond, which turns out to be singly occupied with ON = 1.00 |e|. For the corresponding boron carbonyl complex monocations, as demonstrated, Fig. 3C and D show the bonding patterns of C_s $B_{20}(CO)_4^+$ and D_2 $B_{20}(CO)_8^+$ on their DR tubular B_{20} frameworks, respectively. Obviously, the 20 2c-2e localized σ-bonds formed on the two B_{10} rings and 5 20c-2e σ + σ delocalized σ-bonds and 5 20c-2e π + π delocalized π-bonds formed positively over the DR tubular B_{20} framework in D_{2d} B_{20}^+ (Fig. 3B) have all been practically well inherited in both C_s $B_{20}(CO)_4^+$ and D_2 $B_{20}(CO)_8^+$, though with slightly lower ON values. Similar bonding patterns exist in the whole $B_{20}(CO)_n^+$ and $B_{20}(CO)_n$ species (n = 1–8), as depicted in Fig. S21–S28.

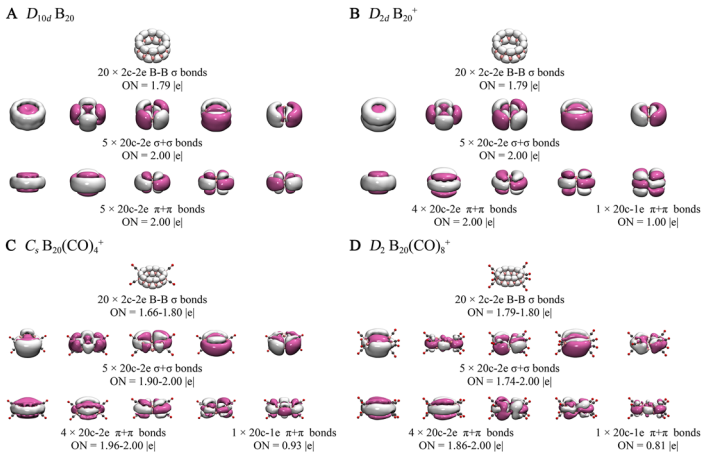

Fig. 3 AdNDP bonding patterns of the DR tubular D_{10d} B_{20} (A), D_{2d} B_{20}^+ (B), C_s $B_{20}(CO)_4^+$ (C), and D_2 $B_{20}(CO)_8^+$ (D) on the B_{20} DR tubular frameworks, with the occupation numbers (ON) indicated.

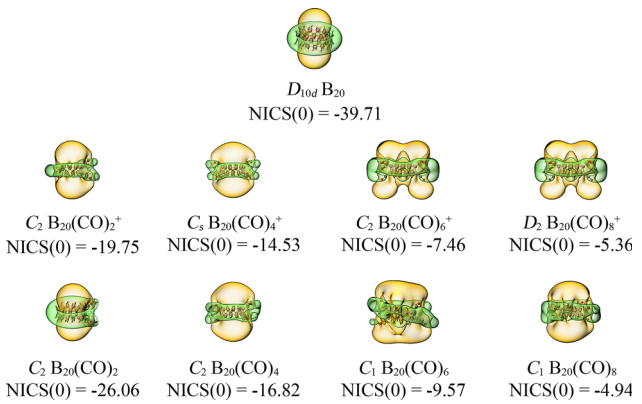

Fig. 4 Calculated ICSS surfaces of D_{10d} B_{20}, C_2 $B_{20}(CO)_2^+$, C_s $B_{20}(CO)_4^+$, C_2 $B_{20}(CO)_6^+$, D_2 $B_{20}(CO)_8^+$, C_2 $B_{20}(CO)_2$, C_2 $B_{20}(CO)_4$, C_1 $B_{20}(CO)_6$, and C_1 $B_{20}(CO)_8$ at the PBE0 level, with the calculated nuclear independent chemical shift values at the centres of the DR tubular B_{20} tubes (NICS(0)) indicated in ppm. The yellow and green areas with negative and positive $NICS_{zz}$ values represent the shielding and de-shielding regions, respectively.

To comprehend the overall aromaticity of these DR tubular systems, Fig. 4 depicts the calculated ICSS surfaces of $B_{20}(CO)_n^+$ and $B_{20}(CO)_n$ (n = 2, 4, 6, 8) series, compared with that of the perfect DR D_{10d} B_{20} on the top, which is known to possess typical tubular aromaticity.[20,52,53] Interestingly, both the $B_{20}(CO)_n^+$ and $B_{20}(CO)_n$ series exhibit similar ICSS surfaces with that of D_{10d} B_{20}, where the yellow areas with negative NICS-ZZ values inside the B_{20} tube and within about 1.0 Å above the tube in the vertical direction belong to the chemical shielding regions, while the green regions with positive NICS-ZZ values like a belt around the B_{20} tube in horizontal directions belong to the chemical de-shielding regions. More specifically, $B_{20}(CO)_n^+$ and $B_{20}(CO)_n$ (n = 2, 4, 6, 8) possess the negative nuclear independent chemical shift values of NICS = −19.75, −14.53, −7.46, and −5.36 and NICS = −26.06, −16.82, −9.57, and −4.94 ppm at the centres of the DR B_{20} tubes, respectively. Similar ICSSs exist in other $B_{20}(CO)_n^+$ and $B_{20}(CO)_n$ (n = 1, 3, 5, 7) series (Fig. S30). These results indicate that, similar to DR tubular D_{10d} B_{20}, which has the largest negative NICS value of −39.71 ppm at the centre, both the distorted DR tubular $B_{20}(CO)_n$ neutrals and $B_{20}(CO)_n^+$ monocations (n = 1–8) exhibit tubular aromaticity, rendering extra-stability to help stabilize these DR tubular complexes. As indicated in Fig. S31, the calculated ring current maps of the slightly or severely distorted DR tubular $B_{20}(CO)_n^+$ and $B_{20}(CO)_n$ (n = 2, 4, 6, 8) using the ACID approach[44] further evidence the tubular aromaticity of the systems.

Effective σ-donations and weak π-back-donations

Detailed EDA-NOCV analyses in Fig. 5 and Tables S1, S2 reveal the corresponding deformation densities $\Delta\rho$ and shapes of the most important interacting orbitals of the pairwise orbital interactions depicted of C_s $B_{20}(CO)^+$ and C_s $B_{20}(CO)$, more specifically, with D_{2d} B_{20}^+ and CO and D_{10d} B_{20} and CO as reacting fragments, respectively. Obviously, one effective

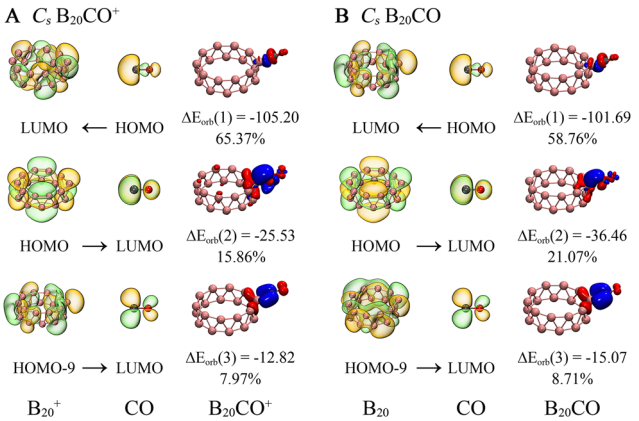

Fig. 5 Plots of the deformation densities ($\Delta\rho$) and shapes of the most important interacting orbitals of the pairwise orbital interactions between B_{20}^+ and CO in C_s $B_{20}CO^+$ (A) and B_{20} and CO in C_s $B_{20}CO$ (B), with the orbital interaction energies (ΔE_{orb}) in kcal mol^{-1} and their percentage contributions to the overall orbital interactions indicated. The colour code of the charge flow is from red to blue.

σ-donation from the HOMO of CO to the LUMO of B_{20}^+ in radial direction, which contributes 65.37% to the overall orbital interaction (ΔE_{orb} = −105.2 kcal mol^{-1}) between B_{20}^+ and CO and two weak π-back-donations perpendicular to each other from the HOMO and HOMO−9 of B_{20}^+ to the two degenerate LUMOs of CO, which contribute 15.86% and 7.97% (Fig. 5A), respectively, coexist in the coordination interactions of C_s $B_{20}(CO)^+$, with the dominant σ-donation bond being well reflected in the AdNDP 2c-2e B–C σ-bond in Fig. S21. As shown in the red → blue charge flow colour code, the doubly occupied σ-HOMO of CO serves as a lone-pair donor in the effective σ-donation interaction, while the two unoccupied degenerate antibonding π*-LUMOs of CO perpendicular to each other function as electron acceptors in the two weak π-back-donations. Similarly, one effective σ-donation, which contributes 58.76% to the overall orbital interactions and two weak π-back-donations, which contribute 21.07% and 8.71%, respectively, coexist in C_s $B_{20}(CO)$, as clearly shown in Fig. 5B.

Similar coordination bonding patterns exist in the whole $B_{20}(CO)_n^{+/0}$ series between the CO ligands and the DR tubular B_{20} core. The effective B_{20} ← CO σ-donations and weak B_{20} → CO π-back-donations in these boron carbonyl complexes appear to be similar to that of the TM–CO coordination interactions in classic TM carbonyl complexes, indicating that the peripheral boron atoms in these DR tubular boron carbonyl complexes can also be viewed as "honorable transition metals",[4,5] similar to the situations observed in the previously reported 2D $B_{13}(CO)_n^+$, $B_{11}(CO)_n$, and $B_{15}(CO)_n^+$.[17,18]

Conclusions

Extensive chemisorption experiments and first-principles theory calculations performed in this work indicate that previously experimentally observed gas-phase DR tubular D_{2d} B_{20}^+ can chemisorb up to eight CO molecules consecutively under ambient conditions to form a series of DR tubular boron carbonyl monocations $B_{20}(CO)_n^+$ (n = 1–8), unveiling the emergence of a 2D-to-3D transition in boron carbonyl complexes. Both DR tubular $B_{20}(CO)_n^+$ and their neutral counterparts $B_{20}(CO)_n$ appear to be tubularly aromatic in nature. Further joint experimental and theoretical investigations on larger boron carbonyl complexes $B_m(CO)_n^{+/-}$, which may have a 3D cage-like, bilayer and core–shell structures, are currently in progress. Carbonyl coordination is expected to be an effective approach to stabilize boron nanoclusters and low-dimensional nanomaterials to further enrich the chemistry of boron.

Conflicts of interest

There are no conflicts to declare.

Data availability

All the data are available online on the website of PCCP.

All the necessary low-lying isomers and their chemisorption pathways, bonding patterns, ICSS surfaces, ring currentmaps, and EDA-NOCV analyses provided. See DOI: https://doi.org/10.1039/d5cp01827g

Acknowledgements

This work was supported by the National Natural Science Foundation of China (Grant No. 22003034, 22373061, and 92461303).

References

1 M. F. Zhou, L. Andrews and C. W. Bauschlicher, Jr., *Chem. Rev.*, 2001, **101**, 1931.
2 Q. Q. Tian, X. Yin, R. J. Sun, X. F. Wu and Y. H. Li, *Coord. Chem. Rev.*, 2023, **475**, 214900.
3 A. M. Ricks, Z. E. Reed and M. A. Duncan, *J. Mol. Spectrosc.*, 2011, **266**, 63.
4 X. Wu, L. Zhao, J. Jin, S. Pan, W. Li, X. Jin, G. Wang, M. Zhou and G. Frenking, *Science*, 2018, **361**, 912.
5 S. K. Purkayastha, S. S. Rohman, P. Parameswaran and A. K. Guha, *Phys. Chem. Chem. Phys.*, 2024, **26**, 12573.
6 A. B. Burg and H. I. Schlesinger, *J. Am. Chem. Soc.*, 1937, **59**, 780.
7 M. Zhou, N. Tsumori, L. Andrews and Q. A. Xu, *J. Phys. Chem. A*, 2003, **107**, 2458.
8 M. Zhou, N. Tsumori, Z. Li, K. Fan, L. Andrews and Q. Xu, *J. Am. Chem. Soc.*, 2002, **124**, 12936.
9 M. Zhou, Z. X. Wang, P. V. R. Schleyer and Q. Xu, *ChemPhysChem*, 2003, **4**, 763.
10 T. R. Burkholder and L. Andrews, *J. Phys. Chem.*, 1992, **96**, 10195.
11 M. Zhou, Q. Xu, Z. X. Wang and P. V. R. Schleyer, *J. Am. Chem. Soc.*, 2002, **124**, 14854.
12 J. Y. Jin, G. J. Wang and M. F. Zhou, *Chin. J. Chem. Phys.*, 2016, **29**, 47.
13 J. Jin, G. Wang and M. Zhou, *J. Phys. Chem. A*, 2018, **122**, 2688.
14 J. Jin, G. Wang, M. Zhou, D. M. Andrada, M. Hermann and G. Frenking, *Angew. Chem., Int. Ed.*, 2016, **55**, 2078.
15 J. Jin and M. Zhou, *Dalton Trans.*, 2018, **47**, 17192.
16 Y. Zhao, T. Wang, C. Wang, Z. Zhang, H. Zheng, S. Jiang, W. Yan, H. Xie, G. Li, J. Yang, G. Wu, W. Zhang, D. Dai, X. Zheng, H. Fan, L. Jiang, X. Yang and M. Zhou, *ChemPhysChem*, 2022, **23**, e202200060.
17 R. N. Yuan, J. J. Chen, Q. Chen, Q. W. Zhang, H. Niu, R. Wei, Z. H. Wei, X. N. Li and S. D. Li, *J. Am. Chem. Soc.*, 2024, **146**, 31464.
18 R. N. Yuan, Q. Chen, H. Niu, C. Y. Gao, X. N. Zhao, Y. B. Wu, S. G. He and S. D. Li, *Phys. Chem. Chem. Phys.*, 2025, **27**, 7279.
19 J. Wang, W. Fan, S. B. Cheng and J. Chen, *J. Phys. Chem. A*, 2024, **128**, 7869.

20 B. Kiran, S. Bulusu, H. J. Zhai, S. Yoo, X. C. Zeng and L. S. Wang, *Proc. Natl. Acad. Sci. U. S. A.*, 2005, **102**, 961.
21 W. An, S. Bulusu, Y. Gao and X. C. Zeng, *J. Chem. Phys.*, 2006, **124**, 154310.
22 T. B. Tai, N. M. Tam and M. T. Nguyen, *Chem. Phys. Lett.*, 2012, **530**, 71.
23 E. Oger, N. R. M. Crawford, R. Kelting and P. Weis, *Angew. Chem., Int. Ed.*, 2007, **46**, 8503.
24 X. N. Wu, B. Xu, J. H. Meng and S. G. He, *Int. J. Mass Spectrom.*, 2012, **310**, 57.
25 Z. Yuan, Y. X. Zhao, X. N. Li and S. G. He, *Int. J. Mass Spectrom.*, 2013, **354**, 105.
26 R. A. J. O'Hair, *Chem. Commun.*, 2006, 1469.
27 L. D. Socaciu, J. Hagen, U. Heiz, T. M. Bernhardt, T. Leisner and L. Wöste, *Chem. Phys. Lett.*, 2001, **340**, 282.
28 Z. Yuan, Z. Y. Li, Z. X. Zhou, Q. Y. Liu, Y. X. Zhao and S. G. He, *J. Phys. Chem. C*, 2014, **118**, 14967.
29 C. Adamo and V. Barone, *J. Chem. Phys.*, 1999, **110**, 6158.
30 R. Krishnan, J. S. Binkley, R. Seeger and J. A. Pople, *J. Chem. Phys.*, 1980, **72**, 650.
31 M. J. Frisch, G. W. Trucks, H. B. Schlegel, G. E. Scuseria, M. A. Robb, J. R. Cheeseman, G. Scalmani, V. Barone, B. Mennucci, G. A. Petersson, *et al.*, *Gaussian 16, Revision C.01*, Gaussian, Inc., Wallingford, CT, USA, 2016.
32 Q. Chen, W. L. Li, Y. F. Zhao, S. Y. Zhang, H. S. Hu, H. Bai, H. R. Li, W. J. Tian, H. G. Lu, H. J. Zhai, S. D. Li, J. Li and L. S. Wang, *ACS Nano*, 2015, **9**, 754.
33 H. J. Zhai, Y. F. Zhao, W. L. Li, Q. Chen, H. Bai, H. S. Hu, Z. A. Piazza, W. J. Tian, H. G. Lu, Y. B. Wu, Y. W. Mu, G. F. Wei, Z. P. Liu, J. Li, S. D. Li and L. S. Wang, *Nat. Chem.*, 2014, **6**, 727.
34 J. Tian, X. N. Chen, S. D. Li, A. I. Boldyrev, J. Li and L. S. Wang, *Chem. Soc. Rev.*, 2019, **48**, 3550.
35 C. Gonzalez and H. B. Schlegel, *J. Chem. Phys.*, 1989, **90**, 2154.
36 C. Gonzalez and H. B. Schlegel, *J. Phys. Chem.*, 1990, **94**, 5523.
37 S. Grimme, S. Ehrlich and L. Goerigk, *J. Comput. Chem.*, 2011, **32**, 1456.
38 Y. Guo, C. Riplinger, U. Becker, D. G. Liakos, Y. Minenkov, L. Cavallo and F. Neese, *J. Chem. Phys.*, 2018, **148**, 011101.
39 F. Neese, *Wiley Interdiscip. Rev.: Comput. Mol. Sci.*, 2022, **12**, e1606.
40 N. V. Tkachenko and A. I. Boldyrev, *Phys. Chem. Chem. Phys.*, 2019, **21**, 9590.
41 D. Y. Zubarev and A. I. Boldyrev, *Phys. Chem. Chem. Phys.*, 2008, **10**, 5207.
42 T. Lu and F. Chen, *J. Comput. Chem.*, 2012, **33**, 580.
43 W. Humphrey, A. Dalke and K. Schulten, *J. Mol. Graph.*, 1996, **14**, 33.
44 D. Geuenich, K. Hess, F. Köhler and R. Herges, *Chem. Rev.*, 2005, **105**, 3758–3772.
45 Povray, Persistence of vision raytracer, POV-Ray 3.7, **https://www.povray.org/**.
46 T. Ziegler and A. Rauk, *Theor. Chim. Acta*, 1977, **46**, 1.
47 M. P. Mitoraj, A. Michalak and T. Ziegler, *J. Chem. Theory Comput.*, 2009, **5**, 962.
48 M. Mitoraj and A. Michalak, *Organometallics*, 2007, **26**, 6576.
49 G. T. E. Velde, F. M. Bickelhaupt, E. J. Baerends, C. F. Guerra, S. J. A. Van Gisbergen, J. G. Snijders and T. Ziegler, *J. Comput. Chem.*, 2001, **22**, 931.
50 E. VanLenthe, E. J. Baerends and J. G. Snijders, *J. Chem. Phys.*, 1993, **99**, 4597.
51 I. A. Popov, T. Jian, G. V. Lopez, A. I. Boldyrev and L. S. Wang, *Nat. Commun.*, 2015, **6**, 8654.
52 H. J. Zhai, B. Kiran, J. Li and L. S. Wang, *Nat. Mater.*, 2003, **2**, 827.
53 M. P. Johansson, *J. Phys. Chem. C*, 2009, **113**, 524.